

# Re-examining Larson's Scaling Laws in Galactic Molecular Clouds

Mark Heyer<sup>1</sup>, Coleman Krawczyk<sup>1,2</sup>, Julia Duval<sup>3</sup>, James M. Jackson<sup>3</sup>

## ABSTRACT

The properties of Galactic molecular clouds tabulated by Solomon et al (1987) (SRBY) are re-examined using the Boston University-FCRAO Galactic Ring Survey of  $^{13}\text{CO}$  J=1-0 emission. These new data provide a lower opacity tracer of molecular clouds and improved angular and spectral resolution than previous surveys of molecular line emission along the Galactic Plane. We calculate GMC masses within the SRBY cloud boundaries assuming LTE conditions throughout the cloud and a constant  $\text{H}_2$  to CO abundance, while accounting for the variation of the  $^{12}\text{C}/^{13}\text{C}$  with Galacto-centric radius. The LTE derived masses are typically five times smaller than the SRBY virial masses. The corresponding median mass surface density of molecular hydrogen for this sample is  $42 \text{ M}_\odot \text{pc}^{-2}$ , which is significantly lower than the value derived by SRBY (median  $206 \text{ M}_\odot \text{pc}^{-2}$ ) that has been widely adopted by most models of cloud evolution and star formation. This discrepancy arises from both the extrapolation by SRBY of velocity dispersion, size, and CO luminosity to the 1K antenna temperature isophote that likely overestimates the GMC masses and our assumption of constant CO abundance over the projected area of each cloud. The true surface density of clouds likely falls within the range  $80\text{-}120 \text{ M}_\odot \text{pc}^{-2}$ . From velocity dispersions derived from the  $^{13}\text{CO}$  data, we find that the coefficient of the cloud structure functions,  $v_\circ = \sigma_v/R^{1/2}$ , is not constant, as required to satisfy Larson's scaling laws, but rather systematically varies with the surface density of the cloud as  $\sim \Sigma^{0.5}$  as predicted for magnetically supported molecular clouds (Mouschovias 1987).

*Subject headings:* ISM: clouds – ISM: kinematics and dynamics

---

<sup>1</sup>Department of Astronomy, University of Massachusetts, Amherst, MA 01003-9305; heyer@astro.umass.edu

<sup>2</sup>Department of Physics, Drexel University, Philadelphia, PA 19104

<sup>3</sup>Institute for Astrophysical Research, Boston University, Boston, MA 02215

## 1. Introduction

Giant molecular clouds (GMCs) in galaxies are fundamental ingredients to recipes of star formation in galaxies. Their evolution and conversion of interstellar material into stars are governed by the interplay between self-gravity, magneto-turbulent pressure, and feedback processes from newborn stars (McKee 1989). The configuration of a GMC, parameterized by its observed size, velocity dispersion, and mass surface density, offers a snapshot view of its dynamical state. Larson (1981) identified scaling relationships between these observable quantities that have provided the basic, grounding point for all subsequent descriptions of interstellar molecular clouds and star formation. These scaling laws are: 1) a power law relationship between the velocity dispersion and the spatial scale of the emitting volume, 2) self-gravitational equilibrium, and 3) constant gas surface density. The original compilation of these scaling laws used molecular line data available from earlier studies. Many of these data were collected with the earliest millimeter wave telescopes and instrumentation and included spatially undersampled maps of molecular line emission with poor sensitivity, compared to currently available data, from a limited number of nearby ( $< 2.2$  kpc) interstellar clouds.

The Larson scaling laws have been supplemented with additional observations with improved sensitivity and larger samples. The most significant study to confirm Larson’s results is described by Solomon et al (1987) (hereafter, SRBY). They used the University of Massachusetts-Stony Brook (UMSB) Galactic Plane Survey (Sanders et al 1985) to identify 273 GMCs in the first quadrant. Each cloud was defined as a closed surface within the longitude-latitude-velocity data cube at a given threshold of antenna temperature. For most entries in the catalog, the threshold was 4 K ( $T_R^*$ ). This high threshold, relative to the noise of the data, was necessary to avoid the blending of emission at lower intensity levels from unrelated clouds that are densely distributed within the  $l - b - V_{LSR}$  domain of the spectroscopic observations. The blending is particularly severe near the tangent points at each Galactic longitude. Realizing that such a high threshold would not fully account for the bulk of the emission from a GMC, SRBY extrapolated the sizes, velocity dispersions, and CO luminosities to the 1 K isophote. After accounting for this low level contribution and its effect on the tabulated properties, SRBY identified a size-linewidth relationship with a steeper power law index (0.5) than derived by Larson (1981) and concluded that GMCs are self-gravitating objects in virial equilibrium. An algebraic consequence of these two results is that the molecular gas surface density is constant for all clouds with  $\Sigma(H_2) = 206 \text{ M}_\odot \text{pc}^{-2}$ . This value is corrected from  $170 \text{ M}_\odot \text{pc}^{-2}$  quoted in SRBY to account for the difference in the values adopted for the Galactocentric radius of the Sun (10 kpc vs 8.5 kpc) that affects the virial mass. We have similarly corrected other values in the SRBY catalog (CO luminosity, distance, galactocentric radius, sizes) using the rotation curve of Clemens (1985).

The data used by Larson (1981) and SRBY are not optimal for deriving properties of interstellar clouds. In both cases, the observed cloud fields were spatially undersampled with respect to the angular resolution of the telescope used to gather the CO data. Owing to poor sensitivity or the need for identifying clouds at a high intensity threshold, the target clouds are biased towards the brightest interstellar clouds, the brightest regions within the clouds, or ones that happen to be nearby or associated with conspicuous star formation. In the case of SRBY, the tracer of molecular gas was  $^{12}\text{CO}$  J=1-0 line emission that is optically thick under most prevailing conditions in molecular clouds. Given these limitations, it is reasonable to inquire whether the properties of GMCs and the corresponding Larson scaling laws can withstand scrutiny with vastly superior data available today. For example, a recent study by Bolatto et al (2008) examined the properties of resolved giant molecular clouds in dwarf galaxies and those within Local Group spiral galaxies. They found the properties of extragalactic GMCs similar to those determined by SRBY for Galactic GMCs.

The Boston University-FCRAO Galactic Ring Survey (GRS) imaged the  $^{13}\text{CO}$  J=1-0 emission between Galactic longitudes  $18^\circ$  and  $56^\circ$  and latitudes,  $|b| \leq 1^\circ$  with the FCRAO 14m telescope (Jackson et al 2006). The advantages of the GRS over the UMSB survey includes higher angular sampling and spectral resolution and the use of a mostly optically thin tracer of molecular gas. The lower opacity of  $^{13}\text{CO}$  reduces, but does not fully eliminate, the effect of velocity crowding. It also enables a more direct measure of molecular hydrogen column density and mass under the reasonable assumption of local thermodynamic equilibrium (LTE) (Dickman 1978). These advantages are illustrated in Figure 1, which compares the integrated emission from several clouds identified by SRBY derived from each survey. The UMSB  $^{12}\text{CO}$  data identifies the location, angular extent and velocity of the molecular cloud but is unable to discern any substructure within the cloud. Owing to improved resolution afforded by fully sampling optically thin  $^{13}\text{CO}$  emission, the GRS data provide a more precise distribution of molecular material *within* the field with reduced confusion of signal from unrelated clouds along the line of sight. The angular extent of the  $^{13}\text{CO}$  emission is less than that of the  $^{12}\text{CO}$  line. This reduced size is observed toward most molecular clouds and results from the subthermal excitation of CO within the low density envelopes (Heyer, Carpenter, & Ladd 1996; Carpenter, Snell, Schloerb 1995; Goldsmith et al 2008). The  $^{12}\text{CO}$  J=1-0 line is visible in these regions owing to radiative trapping that maintains sufficient excitation of the upper energy levels. In this study, we examine the properties of the SRBY sample of GMCs using the  $^{13}\text{CO}$  J=1-0 data of the GRS.

## 2. Results

Of the 273 GMCs catalogued by SRBY, 180 fall within the coverage of the GRS. To minimize the fractional error when using kinematic distances, we restrict our analysis to 162 of these GMCs with  $V_{LSR} > 20 \text{ km s}^{-1}$ . For each GMC entry, the SRBY catalogue provides the emission weighted centroid positions,  $(l_p, b_p, v_p)$ , angular extents along the galactic longitude and latitude axes,  $\sigma_l, \sigma_b$ , velocity dispersion,  $\sigma_v$ ,  $^{12}\text{CO}$  luminosity,  $L_{CO}^{SRBY}$ , and virial mass,  $M_v$ , and near/far side resolved distances.

A primary goal in this study is to derive the mass and surface density for each cloud over the same area as SRBY. We consider the area,  $A_1$ , defined by the position centroids,  $l_p, b_p$ , and the extents for each angular axis as listed in the SRBY catalog

$$A_1 = \int_{b_p - 1.7\sigma_b}^{b_p + 1.7\sigma_b} db \int_{l_p - 1.7\sigma_l}^{l_p + 1.7\sigma_l} dl \text{ deg}^2 \quad (1)$$

where the factor, 1.7, comes from the relationship between the area of each cloud and  $\sigma_l, \sigma_b$  described by SRBY. The velocity interval for each cloud is determined from the inspection of the mean  $^{13}\text{CO}$  and  $^{12}\text{CO}$  spectra over the area,  $A_1$ ,

$$\langle T(v) \rangle = \frac{\int dA_1 T(l, b, v)}{\int dA_1} \text{ K} \quad (2)$$

We also derive properties within a secondary area,  $A_2$ , defined as the area within the half power isophote of the peak column density value within the cloud. Typically, this area is 2-4% of the SRBY defined area,  $A_1$ , and corresponds to the high column density central core of the cloud.

For each of the 162 clouds within the GRS field and velocity range, the basic properties are re-calculated using the  $^{13}\text{CO}$  data,  $T(l, b, v)$ . The updated properties include emission weighted centroid positions,  $l_o, b_o, v_o$ , and velocity dispersion,  $\sigma_v$ , derived from the second moment of the mean  $^{13}\text{CO}$  spectrum of the cloud,

$$\sigma_v^2 = \frac{\sum \langle T(v) \rangle (v - v_o)^2}{\sum \langle T(v) \rangle} \text{ km}^2 \text{ s}^{-2} \quad (3)$$

The improved angular and spectral sampling of the GRS data provide a more precise position and velocity of the cloud than those provided in the SRBY catalog values. The recomputed values for this sample of clouds are listed in Table 1.

## 2.1. GMC Masses

The availability of lower opacity  $^{13}\text{CO}$  J=1-0 emission from the GRS affords a more direct calculation of molecular hydrogen column densities and masses than is provided by  $^{12}\text{CO}$ . The  $^{13}\text{CO}$  column density is derived assuming LTE conditions throughout the cloud area,

$$N_{13}(l, b) = 2.6 \times 10^{14} \left( \frac{\tau_o}{1 - \exp(-\tau_o)} \right) \frac{\int T(l, b, v) dv}{(1 - \exp(-5.3/T_x))} \text{ cm}^{-2} \quad (4)$$

where

$$\tau_o = -\ln \left[ 1 - \frac{T_B}{5.3} ((\exp(5.3/T_x) - 1)^{-1} - 0.16)^{-1} \right] \quad (5)$$

(Rohlfs & Wilson 2003). The excitation temperature,  $T_x$ , at each position is determined from the peak temperature of the optically thick  $^{12}\text{CO}$  line of UMSB survey data resampled to the GRS grid over the same target velocity interval.

To relate this column density to the more abundant  $\text{H}_2$  component, one requires the abundance ratio of  $^{12}\text{CO}$  to  $^{13}\text{CO}$  and the ratio of  $^{12}\text{CO}$  to  $\text{H}_2$ . It has long been established that the  $^{12}\text{C}$  to  $^{13}\text{C}$  abundance systematically varies with galactocentric radius,  $R_{gal}$  (Penzias 1980). The most recent characterization of this gradient by Milam et al (2005) is

$$[^{12}\text{C}/^{13}\text{C}] = 6.2R_{gal} + 18.7 \quad (6)$$

This scaling is applied to the  $^{13}\text{CO}$  column density for each cloud according to its Galactocentric radius,  $R_{gal}$ , to derive a  $^{12}\text{CO}$  column density,  $N_{12}(l, b) = [^{12}\text{C}/^{13}\text{C}]N_{13}(l, b)$ . We then derive an  $\text{H}_2$  column density,  $N_{H_2}(l, b)$ , at each grid position, assuming a constant  $\text{H}_2/^{12}\text{CO}$  abundance ratio of  $1.1 \times 10^4$  (Freking, Langer, & Wilson 1982). Under these assumptions, the  $\text{H}_2$  mass,  $M_{LTE}$ , is calculated from integration of the column density distribution,  $N_{H_2}(l, b)$  over each area,  $A_1$  and  $A_2$ ,

$$M_{LTE} = \mu m_{H_2} D^2 \int dA N_{H_2}(l, b) \quad (7)$$

where  $m_{H_2}$  is the mass of molecular hydrogen,  $\mu = 1.36$ , is the mean molecular weight that accounts for the contribution of Helium, and  $D$  is the distance to the cloud. These masses are listed in Table 1.

A comparison of the virial mass,  $M_v$ , listed in the SRBY catalog, with  $M_{LTE}$  within  $A_1$ , is shown in Figure 2. While well correlated, it is clear that the LTE-derived masses are significantly smaller than the SRBY  $^{12}\text{CO}$  virial mass over the same projected area. Typically,  $M_{LTE} \approx M_v/5$ . Given this large discrepancy in GMC masses we summarize the limitations of the SRBY virial mass estimates and the GRS LTE mass estimates.

The SRBY estimates of cloud virial masses rely on the accurate extrapolation of cloud properties,  $\sigma_v$ ,  $R$ , from the values defined at the 4 K or higher threshold of antenna temperature to the 1 K isophote that presumably circumscribes the bulk of the GMC. For such an extrapolation to succeed, the measured variation of the cloud properties (CO luminosity, size, velocity dispersion) with antenna temperature above the 4 K threshold must accurately reflect the structure of the cloud at all antenna temperature values. However, the profile of these values above the 4 K threshold is limited by the angular undersampling of the UMSB survey and the opacity of the CO J=1-0 line. Figure 1 demonstrates that the undersampled UMSB data misses much of the underlying structure of the cloud, especially within the brightest sub-regions, where the cloud is presumably defined at the 4 K limit by SRBY. The primary effect of undersampling the field is aliasing of small scale structure to larger scales. This aliasing necessarily affects the inferred variation of cloud properties with antenna temperature. For example, the 3' sampling with 45'' resolution is unlikely to accurately measure the position and amplitude of localized emission peaks within the cloud yet must assign any detected signal to a solid angle defined by the sampling interval. By not accounting for small scale structure, the falloff of the cloud with antenna temperature is necessarily shallower than the true profile of the cloud or one more accurately derived from Nyquist sampled data. In addition,  $^{12}\text{CO}$  J=1-0 emission is strongly saturated owing to high optical depth. Not only does high opacity obscure underlying cloud structure, but line saturation also flattens the surface brightness profile. The corresponding extrapolation of shallow profiles induced by angular undersampling and high optical depth of the  $^{12}\text{CO}$  line leads to overestimates of cloud sizes and CO luminosities at the 1 K isophote.

A comparison of the extrapolated values of the CO luminosity,  $L_{\text{CO}}^{\text{SRBY}}$ , as listed in the catalog, and a direct measure,  $L_{\text{CO}}$ , determined from direct integration of the UMSB CO intensities within the cloud boundaries and velocity intervals, is shown in Figure 3. The extrapolated values are typically 35% larger than the direct measures of  $L_{\text{CO}}$ . Such higher values are unexpected given that the direct measure should be contaminated by signal from unrelated clouds along the line of sight over the same velocity range. This suggests that the extrapolated values of the CO luminosity are systematically overestimating the true CO luminosity. Similarly, the extrapolated cloud sizes and velocity dispersions that are used to derive the virial mass may also be inappropriate.

Masses and  $\text{H}_2$  column densities assuming LTE are also subject to limitations and uncertainties. Rohlfs & Wilson (2003) note that the LTE method can overestimate the true  $^{13}\text{CO}$  column densities as the optically thick  $^{12}\text{CO}$  line, used to derive the excitation temperature, may be biased to the warm envelope of the cloud that may not be representative of the excitation within the cooler, denser portions of the cloud responsible for the  $^{13}\text{CO}$  emission. Moreover, the excitation of the upper rotational energy levels of CO are likely not

fully thermalized for most of the cloud volume, so the conventional approximation of the partition function,  $\sum_{J=0}^{\infty} (2J+1) \exp(-J(J+1)hB/kT_x) = kT/hB$ , to account for material within the upper excitation states, may not be valid. Owing to its reduced optical depth, the lower rotational levels of  $^{13}\text{CO}$  may be sub-thermally excited in the low density regime of a giant molecular cloud. Figure 1 reveals that  $^{13}\text{CO}$  is not detected in every line of sight within the SRBY cloud boundaries although spatial averaging can reveal the presence of a weak signal. Such weak or absent  $^{13}\text{CO}$  emission from lines of sight where  $^{12}\text{CO}$  is detected is attributed to subthermal excitation of the line owing to the low volume densities in these outer regions. Lee, Snell, & Dickman (1994) demonstrated that the LTE method underestimates the true column density for those lines of sight with mean densities less than  $3000 \text{ cm}^{-3}$  that are insufficient to thermalize the  $^{13}\text{CO}$   $J=1-0$  transition.

The assumed constant abundance of CO relative to molecular hydrogen within a cloud is likely the largest source of error in our application of the LTE method. CO abundances can strongly vary between the strongly self-shielded interiors and the UV exposed envelope owing to selective photodissociation and fractionation (van Dishoeck & Black 1988; Liszt 2007). In a recent study of the Taurus molecular cloud, Goldsmith et al (2008) show that this subthermally excited, UV exposed envelope can contribute as much as 50% of the cloud’s mass when accounting for such molecular abundance variations. By not considering these abundance variations and the effects of subthermal excitation, our LTE derived GMC masses may underestimate the true values.

To more quantitatively examine the impact of subthermal excitation and reduced  $^{13}\text{CO}$  abundances in the outer envelopes of GMCs, we analyze the excitation and radiative transfer through a spherical model cloud using a large velocity gradient (LVG) code to compute  $^{13}\text{CO}$   $J=1-0$  line intensities. These models provide a plausible, but not a unique, set of conditions for material with predicted  $^{13}\text{CO}$  emission that falls below the GRS sensitivity limit ( $5\sigma \sim 1 \text{ K}$ ). Figure 4 displays the variation of  $^{13}\text{CO}$   $J=1-0$  antenna temperature with volume density for gas with kinetic temperature of 15 K, a velocity dispersion of  $2 \text{ km s}^{-1}$ , and two values of  $^{13}\text{CO}$  column density. For densities below  $3000 \text{ cm}^{-3}$ , the  $^{13}\text{CO}$  energy levels are subthermally excited (excitation temperature less than kinetic temperature). The upper curve corresponds to gas with  $\text{H}_2$  column densities of  $10^{22} \text{ cm}^{-2}$ , which is comparable to the value inferred by SRBY and a  $^{13}\text{CO}$  to  $\text{H}_2$  abundance of  $2 \times 10^{-6}$ . For extremely subthermally excited gas with densities less than  $120 \text{ cm}^{-3}$ , the predicted  $^{13}\text{CO}$   $J=1-0$  emission would not be detected by the GRS observations. The lower curve is computed for a  $^{13}\text{CO}$  column density of  $2 \times 10^{15} \text{ cm}^{-2}$  that could result from either  $\text{H}_2$  column densities of  $10^{21} \text{ cm}^{-2}$  and a  $^{13}\text{CO}$  to  $\text{H}_2$  abundance of  $2 \times 10^{-6}$  or  $\text{H}_2$  column densities of  $10^{22} \text{ cm}^{-2}$  and a  $^{13}\text{CO}$  to  $\text{H}_2$  abundance of  $2 \times 10^{-7}$ . The reduced abundance may be expected within cloud envelopes exposed to the ambient UV radiation field. In these cases, the predicted  $^{13}\text{CO}$

emission falls well below the GRS sensitivity limit for all densities.

These simplistic models illustrate that column densities comparable to those inferred by SRBY could be hidden from the GRS observations owing to the effects of subthermal excitation and decreasing abundance of CO relative to H<sub>2</sub> in the outer envelopes of GMCs. However, such conditions are not likely to prevail in the higher density, UV shielded central regions of the cloud where <sup>13</sup>CO is detected. Yet these lines of sight also have lower column densities than those derived by SRBY. Moreover, <sup>13</sup>CO is typically detected within at least 50% of the SRBY defined areas. It would seem rather implausible and gravitationally unstable that these central regions are surrounded by gas with higher surface density.

It is possible that these limitations of the LTE derived masses that respectively lead to overestimates and underestimates of cloud mass may tend to cancel. However, the spatial variation of molecular abundances is expected to have a larger effect. Based on the local cloud example in Taurus and the fraction of area with detectable <sup>13</sup>CO emission within the SRBY boundaries, the LTE derived masses are likely lower limits. The true values of GMC mass could be larger by factors of 2-3, as estimated by Goldsmith et al (2008).

A commonly used validation of the SRBY estimates of cloud masses and surface densities is the consistency with the CO to H<sub>2</sub> conversion factor,  $X_{CO}$ , derived from  $\gamma$ -ray measurements (Strong & Mattox 1996). That is,  $X_{CO} = M_{vir}/L_{CO}^{SRBY} = 4.1 M_{\odot}/(K km s^{-1} pc^2)$ , which corresponds to  $1.9 \times 10^{20}$  H<sub>2</sub> molecules cm<sup>-2</sup>, accounting for the abundance of He. As previously noted, the SRBY values for the CO luminosity may be erroneously overestimated due to angular undersampling and line saturation. The implied SRBY H<sub>2</sub> column density is  $9.7 \times 10^{21}$  cm<sup>-2</sup> corresponding to a <sup>12</sup>CO mean surface brightness within the cloud boundaries of 51 K km s<sup>-1</sup> assuming the CO to H<sub>2</sub> conversion factor. However, the median surface brightness averaged over the area of each cloud,  $\int \int dv dA T(l, b, v) / \int dA$ , is 30 K km s<sup>-1</sup>. This difference is evident for the 3 clouds shown in Figure 1, where the color lookup table for the <sup>12</sup>CO images is set so all pixels above 50 K km s<sup>-1</sup> should be saturated. Only a small fraction of pixels exceed this value. Cloud blending should only increase the mean surface brightness of each cloud. Either the extrapolated SRBY column densities are too large or the <sup>12</sup>CO-H<sub>2</sub> conversion factor is too small to be consistent with the observed surface brightness distributions.

How do the newly derived LTE masses compare with the X factor? The mean value of  $M_{LTE}/L_{CO}$  is  $1.8 M_{\odot}/(K km s^{-1} pc^2)$ . However, the direct measure of  $L_{CO}$  is likely an upper limit due to cloud blending, and  $M_{LTE}$  is a lower limit due to the neglect of subthermal excitation and abundance variations. If  $M_{GMC} \sim 2M_{LTE}$ , as suggested by local cloud studies, then these LTE-derived column density estimates are compatible with the value of  $X_{CO}$  determined from  $\gamma$ -rays.



## 2.2. GMC Surface Densities

The surface density of a molecular cloud is a key property to its evolution and dynamical state (McKee & Ostriker 2007). GMC surface densities are simply the mass of the cloud divided by the projected area. Since we are tabulating masses within the same area as SRBY, the discrepancies in masses, discussed in the previous section, are mirrored in the resultant mass surface densities. The distribution of LTE derived surface densities determined within the SRBY defined areas are shown in Figure 5. Also shown is the distribution of mass surface density values assuming virial equilibrium as determined by SRBY. The median surface density implied by the LTE derived masses is  $42 \text{ M}_{\odot} \text{pc}^{-2}$ . Accounting for subthermal excitation and abundance variations, the surface density could be somewhat larger, 80-120  $\text{M}_{\odot} \text{pc}^{-2}$ .

The distribution of LTE derived mass surface densities is much narrower relative to the SRBY distribution and seemingly consistent with Larson’s third law. There are several reasons to expect a limited variation of GMC surface densities derived from a given gas tracer. First, for a given UV radiation field, there is a minimum column density necessary to self-shield  $\text{H}_2$  and  $^{12}\text{CO}$  in order to build and maintain significant molecular abundances. Secondly, high density regions (cores) within a GMC subtend a small fraction of the projected area of a cloud and do not significantly contribute to the overall mass. Moreover, owing to high optical depths and chemical depletion, such regions are not readily detected by  $^{12}\text{CO}$  or  $^{13}\text{CO}$ . Therefore, one expects to find a limited range of molecular surface densities corresponding to those required for molecular self-shielding within a given UV radiation field (Elmegreen 1989; McKee 1989).

## 3. Discussion

The GMC masses derived in this study are systematically lower than those estimated by SRBY. These lower values have significant implications to the global molecular content of the Galaxy. Solomon & Rivolo (1989) provide a detailed summary of the biases and completeness inherent in their cloud definition. They demonstrate that the SRBY catalog is reasonably complete down to a limiting mass of  $2.5 \times 10^5 \text{ M}_{\odot}$  (corrected for current Galactic distances). Accounting for Malmquist bias effects, they estimate that the SRBY clouds account for 40% of the total CO luminosity of the UMass-Stony Brook Survey coverage. Similarly, they find that 40% of the CO flux comes from SRBY clouds. The remaining 60% of the CO luminosity and flux is presumed to originate from cold and/or small clouds that fall below their GMC identification threshold. The mass distribution,  $dN(M)/dM$ , of GMCs follows a power law,  $dN/dM \sim M^{-\alpha_M}$  with  $\alpha_M$  ranging from 1.5 (SRBY) to 1.8 (Heyer,

Carpenter, & Snell 2001). The measured slopes of the GMC mass function imply that most of the molecular mass in the Galaxy resides within the largest clouds that are included in the SRBY sample. Yet, our new calculations of cloud masses imply that the true masses are smaller than the SRBY values by factors of 2-5 depending on the correction for subthermally excited gas and varying abundances within a cloud. Such a rescaling of GMC masses implies a reduced molecular mass content of the Galaxy by these same factors.

Could there be a significant molecular gas mass component residing within smaller, cooler clouds that were not included in the SRBY catalog? Owing to higher angular resolution, the GRS provides higher sensitivity to smaller clouds. A comparison of the GRS field with SRBY clouds does indeed show both discrete and diffuse features that are not included within the SRBY catalog. Yet, we find that 32% of the  $^{13}\text{CO}$  emission over the GRS field originates within SRBY cloud boundaries, which is comparable to the values estimated by Solomon & Rivolo (1989) for  $^{12}\text{CO}$ . Unless this cold, extended emission is from distant clouds, we conclude that there is no significant component of molecular gas that is unaccounted in the SRBY cloud boundaries.

The molecular gas fraction depends on the both the surface density of the cloud and the ambient radiation field (Elmegreen 1989; van Dishoeck & Black 1988). Significant abundances of  $\text{H}_2$  and CO require sufficient column densities to self-shield. It is possible that the fraction of LTE-derived mass to the SRBY-derived virial masses,  $M_{\text{LTE}}/M_v$ , and the higher SRBY surface densities reflect a more intense ambient radiation field in the inner Galaxy owing to higher star formation activity relative to the Solar neighborhood. In this case, one would expect to find a dependence of this fraction on Galactocentric radius. However, we find no evidence for any variation of this fraction over the range of radii (4.1-8.1 kpc) of the cloud sample.

### 3.1. Re-examing Larson’s Scaling Laws

The scaling laws identified by Larson (1981) have provided a fundamental, observational constraint to descriptions of cloud dynamics and star formation. The study by SRBY seemingly confirmed these scaling laws for a larger sample of molecular clouds distributed throughout the Galaxy. Given the results in the previous section, which demonstrate that the SRBY GMC masses and surface densities are likely overestimates to the true values, it is useful to reexamine the Larson (1981) scaling laws with the new GRS data within the SRBY defined cloud boundaries.

As has been demonstrated by many previous studies, the Larson scaling laws are al-

gebraically linked. Here, we resummairize this coupling to explicitly derive the coefficients that are critical to the interpretation of cloud dynamics. Gravitational equilibrium (Larson’s second law) implies that the observed mass of the cloud,  $M_{obs}$ , is equal to the virial mass,

$$M_{obs} = 5\sigma_v^2 R/G \quad (8)$$

The molecular gas surface density,  $\Sigma$ , of a cloud is simply the  $H_2$  mass divided by the projected area,

$$\Sigma = \frac{M_{obs}}{\pi R^2} \quad (9)$$

Eliminating  $M_{obs}$  and solving for  $\sigma_v$ ,

$$\sigma_v = (\pi G/5)^{1/2} \Sigma^{1/2} R^{1/2} \quad (10)$$

If  $\Sigma$  is approximately constant for all clouds (Larson’s third law), then one recovers the size-line width scaling (Larson’s first law),  $\sigma_v = v_o R^{1/2}$ , with the normalization coefficient

$$v_{o,G} = (\pi G \Sigma/5)^{1/2} \quad (11)$$

$$v_{o,G} = 0.52 \left( \frac{\Sigma}{10^2 M_\odot pc^{-2}} \right)^{1/2} km s^{-1} pc^{-1/2} \quad (12)$$

The coefficient,  $v_{o,G}$ , parameterizes the scaling of velocities within a cloud such that non-thermal pressure balances the self-gravity of the cloud with surface density,  $\Sigma$ .

More generally, the velocity field of an interstellar cloud is described by the structure function that measures the variation of velocity differences of order  $p$ , with spatial scale,  $\tau$ ,

$$S_p(\tau) = \langle |v(\mathbf{x}) - v(\mathbf{x} + \tau)|^p \rangle \quad (13)$$

where the angle brackets denote a spatial average over the observed field. Within the inertial range, the structure function is expected to vary as a power law with  $\tau$ . For  $p=1$ ,

$$S_1(\tau) = \delta v = v_o \tau^\gamma \quad (14)$$

where  $\gamma$  is the scaling exponent and  $v_o$  is the scaling coefficient. The existence of a cloud-to-cloud size-velocity dispersion relationship identified by Larson (1981) and SRBY necessarily implies narrow distributions of the scaling exponent and coefficient respectively for all clouds (Heyer & Brunt 2004). From Monte Carlo modeling of the scatter of the SRBY size-velocity dispersion relationship, Heyer & Brunt (2004) constrained the variation of  $\gamma$  and  $v_o$  between clouds to be less than 20% about the mean values that is indicative of a universal structure function. This universality is also reflected in the structure functions of individual clouds as derived by Brunt (2003) and Heyer & Brunt (2004) using Principal Component Analysis.

The Larson scaling laws are concisely represented within the plane defined by the gas surface density,  $\Sigma$ , and the quantity,  $\sigma_v/R^{1/2}$ , for a set of GMC properties (see equation 10). This representation assumes a scaling exponent of  $1/2$  for the structure function of each cloud so that the ordinate,  $\sigma_v/R^{1/2}$ , is equivalent <sup>4</sup> to the scaling coefficient,  $v_o$ . Absolute adherence to universality and all three of Larson’s scaling laws for a set of clouds would be ideally represented by a single point centered at  $\sigma_v/R^{1/2} = (\pi G \Sigma/5)^{1/2}$  for a constant value of  $\Sigma$ . Given uncertainties in distance and deriving surface densities, one more realistically expects an isotropic cluster of points at this location. In Figure 6, we show the corresponding points derived from the GRS data within the SRBY boundaries (area  $A_1$ ) and the area within the half-power isophote of  $N_{H_2}$  (area  $A_2$ ). The vertical error bars displayed in the legend reflect a 20% uncertainty in the distance to each cloud. As a reference point, the large triangle denotes the location of the SRBY mean values ( $\sigma_v/R^{1/2} = 0.72 \text{ km s}^{-1}$ ;  $\Sigma(H_2) = 206 \text{ M}_\odot \text{ pc}^{-2}$ ). The solid line shows the loci of points assuming gravitationally bound clouds,  $\sigma_v/R^{1/2} = (\pi G/5)^{1/2} \Sigma^{1/2}$  that is nearly identical to the coefficients used by SRBY. For both considered cloud areas, the  $^{13}\text{CO}$  data points are displaced from this loci of virial equilibrium. The median virial parameter,  $\alpha_G = M_{v,13}/M_{LTE}$ , is 1.9, where  $M_{v,13}$  is the virial mass derived from  $^{13}\text{CO}$  data within  $A_1$ . However, if the LTE-derived mass underestimates the true cloud mass by a factor of 2 as suggested in §2, then the derived properties are consistent with a virial parameter of unity for this sample of clouds.

More significantly, Figure 6 reveals a systematic variation of  $v_o = \sigma_v/R^{1/2}$  with  $\Sigma$ . This trend is separately evident for each area,  $A_1$  (open circles) and  $A_2$  (filled circles) and follows the virial equilibrium scaling,  $\Sigma^{1/2}$ . The dependence of  $\sigma_v/R^{1/2}$  on  $\Sigma$  signals a departure from the universality of velocity structure functions of clouds. It implies a necessary modification to Larson’s scaling laws but one that is compatible with the rather basic premise of gravitational equilibrium as described in equation 10. The measured variation of  $v_o$  is larger than the values derived by Heyer & Brunt (2004) owing to the larger intrinsic scatter in the size-velocity dispersion relationship determined from the GRS data.

The dependence of  $\sigma_v/R^{1/2}$  on  $\Sigma$  may not have been recognized in previous studies owing to a limited range of surface densities in the observed samples, or the use of a less reliable tracer of molecular gas column density, or simply not considered given the long-standing acceptance of Larson’s scaling laws. The fidelity of the GRS data provides an excellent relative, if not absolute, measure of gas surface density that allows this relationship to be

---

<sup>4</sup>The velocity dispersion of a cloud is equal to the structure function evaluated at the size of the cloud,  $L \sim 2R$ . Cloud-to-cloud size-velocity dispersion relationships use the full velocity dispersion of the cloud but scaled to the cloud radius,  $R$ . Therefore, the respective definitions for the coefficient may differ by a factor of  $\sim \sqrt{2}$  for  $\gamma = 1/2$ .

recognized. We note that this relationship is algebraically imposed when deriving surface densities from the virial mass,  $\Sigma = M_{vir}/\pi R^2 \propto \sigma_v^2/R$ , as calculated by SRBY. However, as shown in Figure 7, the relationship is even evident in the SRBY defined properties when using the mean  $^{12}\text{CO}$  surface brightness and CO to  $\text{H}_2$  conversion factor as a measure of gas surface density,  $\Sigma = X_{\text{CO}} L_{\text{CO}}^{\text{SRBY}}/\Omega_1 D^2$ , where  $\Omega_1$  is the solid angle of the cloud corresponding to  $A_1$  and  $D$  is the distance. Moreover, it is also present in the sample of extragalactic GMCs tabulated by Bolatto et al (2008) (filled squares in Figure 7). The presence of this scaling within these independent data sets offers a powerful verification to our conclusions that the scaling of velocities in a cloud depends on spatial scale and the mass surface density.

### 3.2. GMC Dynamics

Descriptions of cloud dynamics must consider the nature and origin of the observed supersonic motions in GMCs. While much of the theoretical effort has focused on the scaling exponent of the power spectrum or structure function of the velocity field, the normalization,  $v_o$ , provides an important measure of the amplitude of these motions as it is evaluated at a fixed scale of 1 pc. The apparent invariance of  $v_o$  for GMCs enables its use as a distance indicator (Brunt 2003). Figure 6 illustrates an additional constraint to these descriptions – that for a given cloud, the amplitude of the motions depends on the mass surface density. It is not evident from the present measurements whether this variation of  $v_o$  with  $\Sigma$  is due to varying evolutionary states of the sample clouds or one that reflects different cloud conditions owing to the environmental diversity of the ISM.

For sub-Alfvénic clouds whose neutral gas component is dynamically coupled to the interstellar magnetic field through ion-neutral collisions, the observed motions could arise from the propagation of large amplitude, long wavelength Alfvén waves through the cloud (Arons & Max 1975). In fact, a simple model of magnetically supported clouds in which the cloud surface density equals the magnetic critical surface density,  $\Sigma_c = B/(63G)^{1/2}$ , predicts the trend observed in Figure 6 (Mouschovias 1987; Mouschovias & Psaltis 1995; Mouschovias, Tassis, & Kunz 2006). The observed variation of the coefficient with surface density simply reflects plausible differences of the magnetic field strength between clouds owing to Galactic environments and the support of the cloud by the magnetic field for a given value of  $\Sigma$ . The vertical scatter of values for a given surface density would arise from varying flux-to-mass ratios owing to ambipolar diffusion.

One can speculate on the ability of super-Alfvénic turbulence to account for this observed variation. For super-Alfvénic, isothermal gas, the amplitude of density compressions due to shocks scales as the square of the Mach number. Computational simulations demon-

strate that the probability density function (PDF) of the volume density field follows a log-normal distribution whose width depends on the turbulent Mach number (Ostriker et al. 1999; Padoan & Nordlund 2002). Owing to the critical density to maintain excitation, the  $^{13}\text{CO}$  molecular line observations may be biased toward the positive tail of the log-normal distribution, which would be reflected in the derived mass surface density. In this case, the observed correlation of  $v_o$  with  $\Sigma$  could be qualitatively reproduced. More rigorous computational experiments would be required to verify this effect.

#### 4. Summary

Our re-examination of the properties of GMCs in the Milky Way have identified two new results that challenge the long-standing assumptions of cloud dynamics.

1. The mass surface density of GMCs is lower than previously estimated by SRBY. Assuming a constant abundance of molecular hydrogen to CO within a cloud, the median mass surface is  $42 \text{ M}_{\odot}\text{pc}^{-2}$ . Abundance variations within the outer envelope of clouds could increase the mass surface density to 80-120  $\text{M}_{\odot}\text{pc}^{-2}$ . No dependence of mass surface density is found with galactocentric radius.
2. The normalization of the velocity structure function, derived from the velocity dispersion and the size of each cloud,  $v_o = \sigma_v/R^{1/2}$ , varies with the molecular gas surface density, as  $\Sigma^{1/2}$ . The dependence of this factor on surface density conflicts with Larson’s velocity scaling law and the universality of turbulence within molecular clouds. However, this dependence is consistent with the prediction of Mouschovias (1987) that attributes the observed motions to Alfvén waves and the support of GMCs by the interstellar magnetic field.

This work was supported by NSF grant AST 0540852 to the Five College Radio Astronomy Observatory. The authors acknowledge valuable discussions with Telemachos Mouschovias. We also thank Alberto Bolatto for critical comments and providing the table of extragalactic GMC properties prior to publication.

#### REFERENCES

- Arons, J. & Max, C.E. 1975, *ApJ*, 196, L77
- Bolatto, A.D., Leroy, A.K., Rosolowsky, E., Walter, F., & Blitz, L. 2008, *ApJ*, in press
- Brunt, C.M. 2003, *ApJ*, 584, 293

- Carpenter, J.M., Snell, R.L., & Schloerb, F.P. 1995, *ApJ*, 445, 246
- Clemens, D.P. 1985, *ApJ*, 295, 422
- Dickman, R.L., 1978, *ApJS*, 37, 407
- Freking, M.A., Langer, W.D., & Wilson, R.W. 1982, *ApJ*, 262, 590
- Goldsmith, P.F., Heyer, M.H., Narayanan, G., Snell, R.L., Li, D., & Brunt, C.M. 2008, *ApJ*, 680, 428
- Elmegreen, B.G. 1989, *ApJ*, 338, 178
- Heyer, M.H., Carpenter, J.M., & Ladd, E.F. 1996, *ApJ*, 463, 630
- Heyer, M.H., Carpenter, J.M. & Snell, R.L. 2001, *ApJ*, 551, 852
- Heyer, M.H., & Brunt, C.M. 2004, *ApJ*, 615, L45
- Jackson, J.M., Rathborne, J. M., Shah, R. Y., Simon, R., Bania, T. M., Clemens, D. P., Chambers, E. T., Johnson, A. M., Dormody, M., Lavoie, R., Heyer, M. H. 2006, *ApJS*, 163, 145
- Larson, R.B 1981, *MNRAS*, 194, 809
- Lee, Y., Snell, R.L. & Dickman, R.L. 1994, *ApJ*, 432, 167
- Liszt, H.S. 2007, *AA*, 476, 291
- McKee, C.F. 1989, *ApJ*, 345, 782
- McKee, C.F. & Ostriker, E.C. 2007, *ARA&A*, 45, 565
- Milam, S.N., Savage, C., Brewster, M.A., Ziurys, L.M., Wyckoff, S. 2005, *ApJ*, 634, 1126
- Mouschovias, T.Ch. 1987, in *Physical Processes in Interstellar Clouds*, eds. G.E. Morfill & M. Scholer, (Dordrecht: Reidel), p 453
- Mouschovias, T.Ch. & Psaltis, D. 1995, *ApJ*, 444, L105
- Mouschovias, T.Ch., Tassis, K., & Kunz, M.W. 2006, *ApJ*, 646, 1043
- Ostriker, E.C. Stone, J.M., & Gammie, C.F, 1999, *ApJ*, 546, 980
- Padoan, P. & Nordlund, A. 2002, *ApJ*, 576, 870

- Penzias, A.A. 1980, *Science*, 208, 663
- Rohlfs, K. & Wilson, T.L. 2003, *Tools of Radio Astronomy*, (Berlin: Springer)
- Sanders, D.B., Clemens, D.P., Scoville, N.Z., & Solomon, P.M. 1986, *ApJS*, 60, 1
- Solomon, P.M, Rivolo, A.R., Barrett, J, Yahil, A. (SRBY) 1987, *ApJ*, 319, 730
- Solomon, P.M & Rivolo, A.R. 1989, *ApJ*, 339, 919
- Strong, A.W. & Mattox, J.R. 1996, *AA*, 308, L21
- van Dishoeck, E.F. & Black, J.H. 1988, *ApJ*, 334, 771



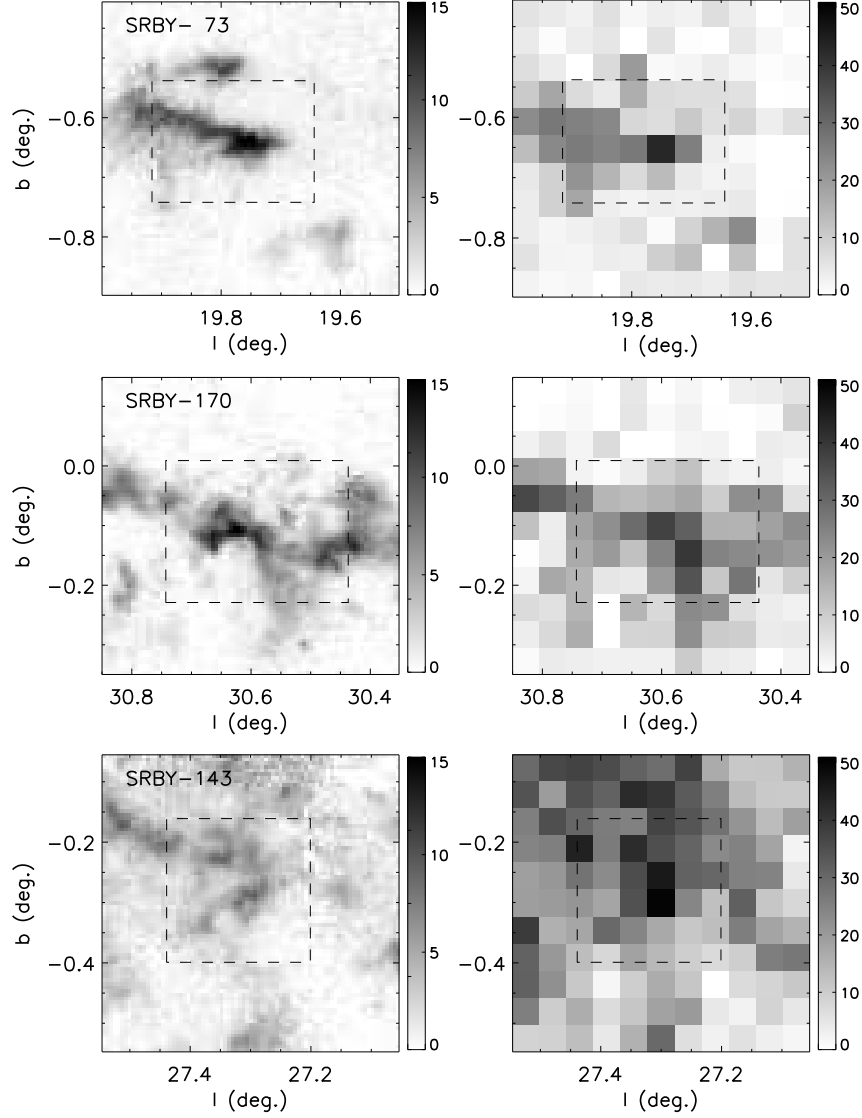


Fig. 1.— (Left) Images of integrated  $^{13}\text{CO}$  J=1-0 emission from the BU-FCRAO Galactic Ring Survey and (Right)  $^{12}\text{CO}$  J=1-0 from the Massachusetts-Stony Brook Survey for 3 giant molecular clouds catalogued by Solomon et al (1987) – (Top) SRBY-73, (Middle) SRBY-170, and (Bottom) SRBY-143. The densely sampled, lower opacity  $^{13}\text{CO}$  line emission offers a more detailed view of cloud structure than is revealed in the undersampled,  $^{12}\text{CO}$  data. The dotted lines show the boundary of each cloud based on the emission centroid and angular sizes given by Solomon et al (1987).

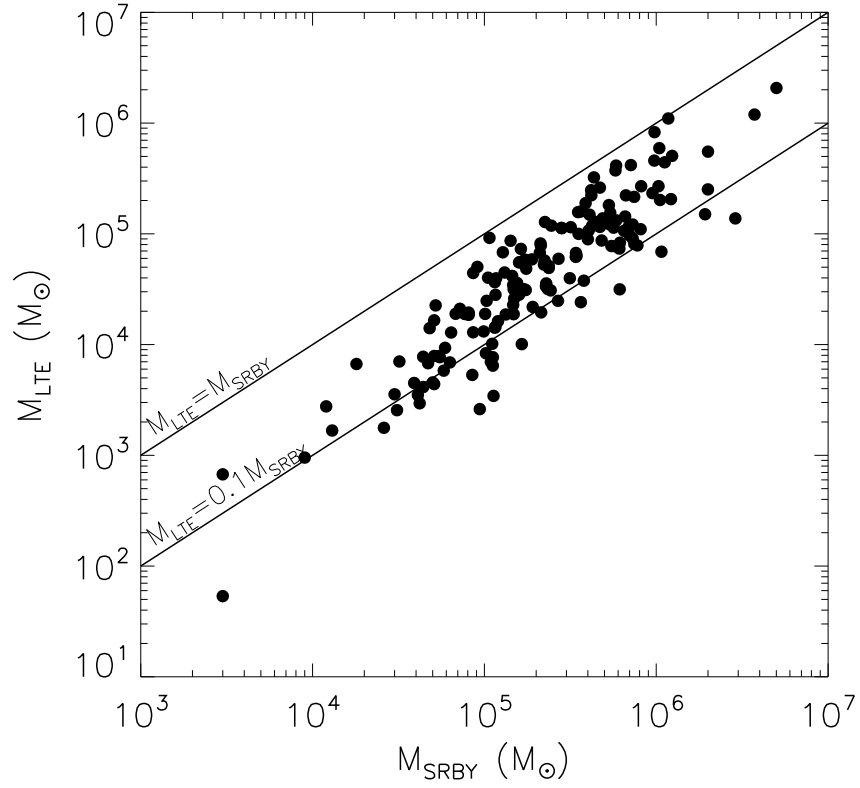


Fig. 2.— A comparison of cloud masses enclosed within the SRBY defined areas calculated from  $^{13}\text{CO}$  assuming LTE with virial masses determined by SRBY. The LTE masses are systematically lower than the SRBY derived virial masses.

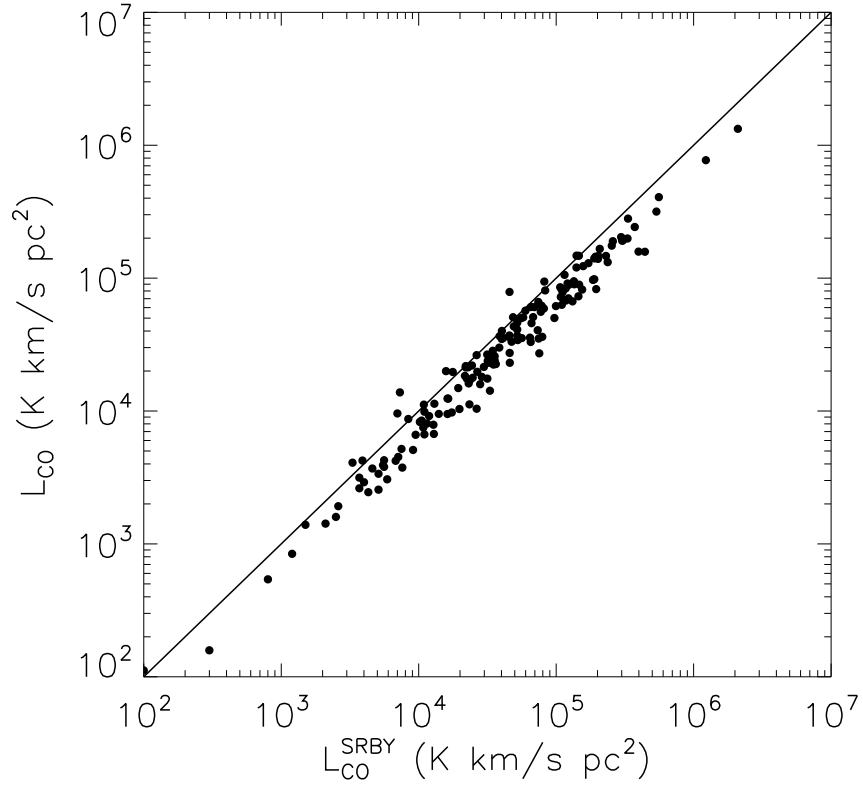


Fig. 3.—  $L_{CO}$  from the direct integration of the signal over the enclosed area versus the CO luminosity from the SRBY catalog. The solid line shows  $L_{CO}^{SRBY} = L_{CO}$ . The smaller direct integration values of  $L_{CO}$  suggest that the extrapolated values overestimate the true value.

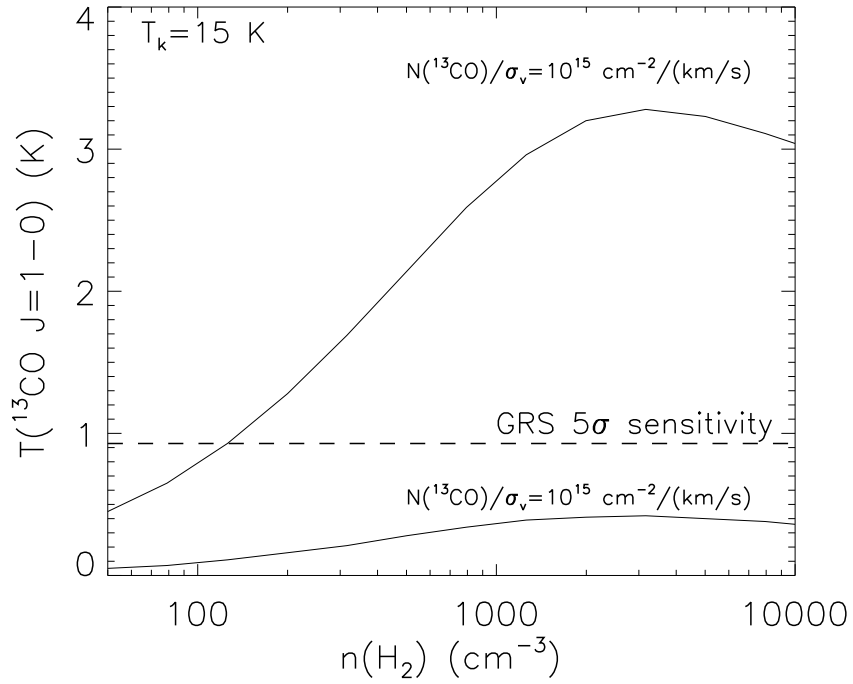


Fig. 4.— The variation of  $^{13}\text{CO}$   $J=1-0$  antenna temperatures with volume density for model clouds with  $^{13}\text{CO}$  column densities of  $2 \times 10^{16} \text{ cm}^{-2}$  and  $2 \times 10^{15} \text{ cm}^{-2}$  and velocity dispersion of  $2.0 \text{ km s}^{-1}$ . These models illustrate conditions within GMC envelopes for which  $^{13}\text{CO}$   $J=1-0$  emission would not be detected by the GRS. High column density ( $10^{22} \text{ cm}^{-2}$ ) material, as derived by SRBY, could be missed by the GRS if these regions have low volume densities ( $< 200 \text{ cm}^{-3}$ ) or low CO to  $\text{H}_2$  abundance ratios.

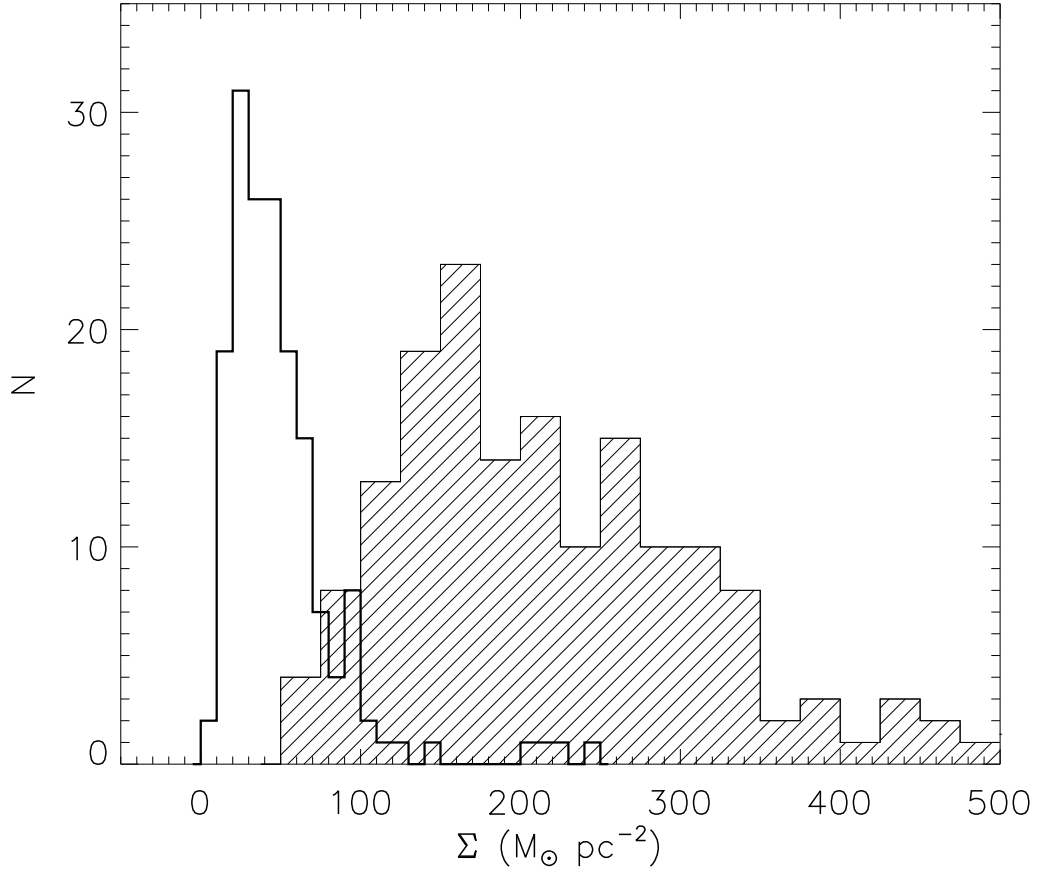


Fig. 5.— The histogram of cloud mass surface densities derived from  $^{13}\text{CO}$  data and assuming LTE and a constant CO to  $\text{H}_2$  abundance ratio within the cloud (heavy line) and mass surface densities determined from virial masses and cloud sizes by SRBY (hashed histogram).

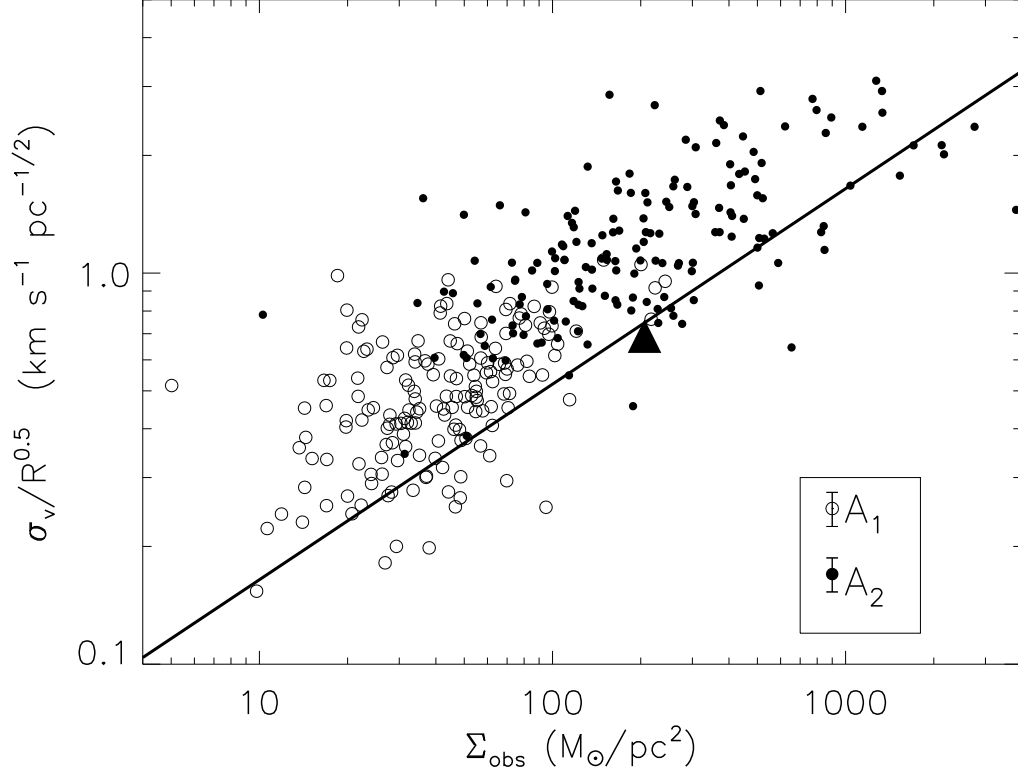


Fig. 6.— The variation of the scaling coefficient,  $v_o = \sigma_v/R^{1/2}$ , with mass surface density derived within the SRBY cloud boundaries (open circles) and the 1/2 maximum isophote of  $\text{H}_2$  column density (filled circles). The filled triangle denotes the value derived by SRBY. The solid line shows the loci of points corresponding to gravitationally bound clouds. There is a dependence of the coefficient with mass surface density in contrast to Larson’s velocity scaling law. The error bars in the legend reflect a 20% uncertainty of the distance to each cloud.

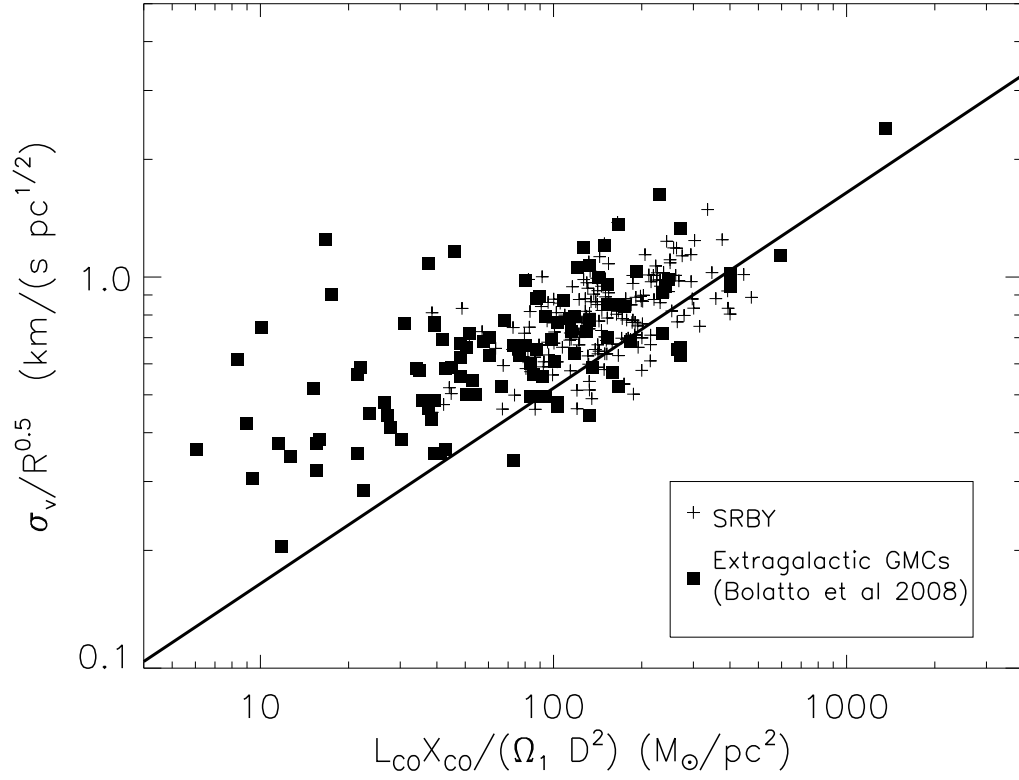


Fig. 7.— The variation of the scaling coefficient,  $v_o = \sigma_v / R^{1/2}$ , with mass surface density for GMCs from the SRBY catalog (+ symbols) and extragalactic GMCs from Bolatto et al (2008) (filled squares).

Table 1. Rederived GMC Properties

SRBY	Within SRBY Defined Area, A <sub>1</sub>									Within Half Max Isophote of N(H <sub>2</sub> ), A <sub>2</sub>			
	$l$ (deg)	$b$ (deg)	$v_o$ (km/s)	$R_g$ (kpc)	Dist (kpc)	$\sigma_v$ (km/s)	R (pc)	$L_{CO}$ ( $Kkm/spc^2$ )	$M_{LTE}$ ( $M_\odot$ )	$\sigma_v$ (km/s)	R (pc)	$L_{CO}$ ( $Kkm/spc^2$ )	$M_{LTE}$ ( $M_\odot$ )
64	18.87	-0.01	47.6	5.0	12.2	2.6	40.6	1.32e+05	3.23e+05	2.0	5.5	3.46e+03	2.88e+04
67	19.22	-0.23	37.2	6.0	13.3	1.5	42.2	8.27e+04	7.86e+04	1.7	5.0	8.94e+02	4.88e+03
68	19.31	0.03	26.0	6.5	2.2	1.9	6.9	3.91e+03	1.41e+04	2.0	0.8	5.58e+01	8.98e+02
70	19.61	-0.08	60.6	4.7	4.2	3.0	9.7	8.28e+03	1.31e+04	2.6	2.3	4.83e+02	2.74e+03
71	19.63	-0.66	56.7	4.9	4.1	2.2	10.3	8.47e+03	1.89e+04	2.2	3.1	8.70e+02	4.47e+03
72	19.67	0.11	25.0	6.5	13.8	2.4	41.3	1.23e+05	2.61e+05	2.2	9.6	7.17e+03	3.54e+04
73	19.78	-0.64	23.8	6.7	2.0	1.3	4.6	8.42e+02	2.77e+03	0.9	0.5	7.73e+00	6.48e+02
74	19.81	-0.39	68.2	4.3	4.7	2.7	32.1	6.30e+04	1.10e+05	2.3	2.3	4.00e+02	3.50e+03
75	19.90	-0.62	44.1	5.4	3.4	2.8	23.2	5.91e+04	1.28e+05	2.3	1.6	3.39e+02	3.64e+03
77	20.58	-0.42	63.3	4.5	11.3	2.9	33.8	6.20e+04	1.21e+05	2.5	2.9	2.60e+02	9.78e+03
78	20.69	-0.32	62.8	4.7	11.5	1.9	22.8	4.10e+04	7.85e+04	1.7	5.2	3.41e+03	1.95e+04
79	20.76	-0.09	57.8	4.8	11.7	3.1	27.1	9.12e+04	1.89e+05	2.6	4.4	3.29e+03	2.48e+04
80	20.75	0.05	78.2	4.2	5.0	3.1	16.7	1.75e+04	1.95e+04	3.0	4.4	1.98e+03	4.92e+03
81	20.87	-0.02	32.3	6.3	13.5	4.0	45.0	1.41e+05	2.33e+05	3.7	11.7	1.34e+04	4.72e+04
82	20.91	-0.31	66.3	4.5	4.6	1.4	15.3	1.61e+04	1.01e+04	1.5	6.1	2.08e+03	4.63e+03
84	21.54	-0.64	53.5	5.1	3.9	2.0	23.7	3.56e+04	4.92e+04	1.6	0.3	9.61e+00	3.76e+02
85	21.71	-0.02	68.3	4.6	4.5	1.9	18.1	2.31e+04	2.41e+04	2.0	5.3	2.31e+03	6.94e+03
86	21.36	0.00	74.4	4.3	10.9	1.7	32.0	7.85e+04	1.19e+05	1.7	6.7	4.28e+03	1.86e+04
87	21.52	0.26	78.8	4.3	5.0	2.2	7.5	4.24e+03	3.50e+03	2.0	1.8	2.59e+02	6.73e+02
88	21.87	-0.36	82.2	4.2	10.6	2.8	46.0	2.04e+05	2.02e+05	2.5	6.0	3.29e+03	1.54e+04
89	22.07	0.17	51.7	5.3	3.6	2.8	22.9	3.69e+04	6.19e+04	1.8	2.0	4.19e+02	2.62e+03
90	22.34	0.08	84.2	4.1	10.4	1.9	18.4	4.62e+04	5.83e+04	1.8	2.0	3.84e+02	4.51e+03
91	22.41	0.33	84.5	4.1	10.4	1.1	17.1	3.66e+04	4.43e+04	1.2	6.9	3.92e+03	2.82e+04
92	22.54	-0.04	115.1	3.3	7.9	0.5	10.6	1.03e+04	3.44e+03	0.5	1.7	1.16e+02	4.63e+02
93	22.56	-0.20	77.4	4.4	10.8	3.1	11.4	3.32e+04	9.20e+04	3.1	8.8	1.27e+04	6.52e+04
94	22.74	-0.24	106.3	3.4	8.7	2.8	16.0	2.26e+04	5.55e+04	3.2	1.2	1.04e+02	2.32e+03
95	22.81	0.41	91.9	3.9	10.0	2.3	19.8	4.58e+04	3.97e+04	2.5	12.8	1.72e+04	2.92e+04
96	22.86	0.40	114.1	3.3	7.8	2.0	6.4	9.59e+03	5.32e+03	2.1	3.9	1.15e+03	3.47e+03
97	23.00	-0.36	76.6	4.5	10.9	2.3	83.4	1.33e+06	2.08e+06	2.2	5.6	6.26e+03	4.99e+04
98	22.97	-0.02	80.2	4.3	10.6	1.6	28.2	1.47e+05	1.21e+05	1.5	2.2	3.27e+02	4.54e+03
99	23.07	0.64	37.2	6.1	2.8	0.8	8.8	1.60e+03	6.68e+03	0.5	0.6	1.21e+01	7.40e+02
100	23.39	-0.23	99.6	3.7	9.3	4.6	23.3	9.70e+04	4.13e+05	4.1	3.0	2.63e+03	3.22e+04
101	23.51	-0.40	74.9	4.6	4.7	1.5	11.6	1.99e+04	1.45e+04	1.6	5.3	2.50e+03	7.03e+03
102	23.55	0.19	87.3	4.3	10.5	5.9	29.8	1.47e+05	4.18e+05	5.8	12.2	3.84e+04	1.35e+05



Table 1—Continued

SRBY	Within SRBY Defined Area, A <sub>1</sub>									Within Half Max Isophote of N(H <sub>2</sub> ), A <sub>2</sub>			
	$l$ (deg)	$b$ (deg)	$v_o$ (km/s)	$R_g$ (kpc)	Dist (kpc)	$\sigma_v$ (km/s)	R (pc)	$L_{CO}$ ( $Kkm/spc^2$ )	$M_{LTE}$ ( $M_\odot$ )	$\sigma_v$ (km/s)	R (pc)	$L_{CO}$ ( $Kkm/spc^2$ )	$M_{LTE}$ ( $M_\odot$ )
103	23.68	0.52	83.2	4.3	5.1	2.0	9.7	4.22e+03	5.81e+03	1.9	2.8	7.86e+02	2.45e+03
105	23.96	0.14	80.9	4.5	5.0	2.1	8.2	1.12e+04	2.10e+04	2.2	2.2	6.33e+02	4.56e+03
106	24.21	-0.04	88.4	4.2	10.1	1.8	22.7	6.06e+04	8.19e+04	2.1	3.8	1.77e+03	9.05e+03
107	24.45	-0.80	58.4	5.3	3.8	1.6	5.7	3.15e+03	4.55e+03	1.9	3.9	1.35e+03	3.57e+03
109	24.49	0.20	36.4	6.2	12.8	1.7	25.4	3.54e+04	5.27e+04	2.1	7.8	4.99e+03	2.12e+04
110	24.39	-0.24	56.1	5.1	11.5	2.7	19.3	3.62e+04	1.19e+05	2.6	10.5	1.49e+04	6.43e+04
111	24.50	-0.15	44.9	5.9	3.1	1.7	9.7	1.24e+04	2.48e+04	1.9	2.5	7.56e+02	4.02e+03
112	24.42	-0.41	44.3	5.9	3.1	0.9	20.2	2.72e+04	3.77e+04	1.1	0.4	5.76e+00	2.47e+02
113	24.49	-0.72	48.6	5.7	3.2	1.0	9.1	5.09e+03	7.69e+03	1.0	1.2	6.61e+01	6.19e+02
114	24.51	-0.23	96.6	3.9	9.3	2.5	26.4	6.83e+04	1.16e+05	2.5	5.4	4.48e+03	2.06e+04
115	24.54	-0.50	60.6	5.1	4.0	1.9	12.0	1.78e+04	4.17e+04	2.0	5.8	3.30e+03	1.76e+04
116	24.63	-0.14	83.8	4.4	10.3	2.1	25.8	8.20e+04	6.89e+04	2.6	5.8	3.69e+03	1.16e+04
117	24.67	-0.05	110.3	3.5	7.7	3.0	26.3	3.70e+04	1.13e+05	2.1	1.4	1.50e+02	9.43e+03
118	25.18	0.16	103.1	3.8	9.0	3.9	23.3	8.08e+04	1.19e+05	3.4	4.5	2.60e+03	1.32e+04
119	25.27	0.33	45.1	5.8	12.2	1.8	34.7	1.06e+05	9.07e+04	1.3	1.5	8.48e+01	4.16e+03
120	25.54	-0.39	116.3	3.7	7.7	1.8	7.3	3.75e+03	4.40e+03	1.7	3.4	5.34e+02	2.24e+03
121	25.40	-0.24	58.2	5.0	11.2	4.1	52.0	1.58e+05	5.94e+05	3.3	1.4	1.77e+02	4.75e+03
122	25.63	-0.11	94.2	4.2	9.7	2.5	53.7	4.07e+05	5.52e+05	2.2	8.0	7.84e+03	5.20e+04
123	25.54	-0.21	118.1	3.7	7.7	1.7	16.3	1.12e+04	1.87e+04	1.3	1.7	2.07e+02	1.73e+03
124	25.79	0.56	46.3	5.8	3.2	1.8	17.9	1.04e+04	3.16e+04	1.8	6.0	2.22e+03	8.27e+03
125	25.72	0.24	110.7	3.8	8.5	2.0	42.7	1.92e+05	1.50e+05	2.0	5.3	3.82e+03	2.12e+04
126	25.91	0.22	69.6	4.9	4.4	1.3	7.2	4.09e+03	3.55e+03	1.5	2.8	3.33e+02	1.05e+03
127	25.71	-0.15	106.3	3.8	8.5	2.1	34.0	6.78e+04	1.15e+05	2.1	3.7	1.26e+03	4.39e+03
128	25.90	-0.13	104.8	3.9	8.7	2.5	37.4	1.75e+05	2.06e+05	3.1	7.0	4.33e+03	1.68e+04
129	25.96	-0.57	62.0	5.2	4.1	1.4	9.6	4.51e+03	4.14e+03	1.5	3.2	4.26e+02	1.11e+03
130	26.18	0.13	70.5	4.9	4.5	1.5	12.8	7.88e+03	1.02e+04	1.5	5.9	2.05e+03	5.45e+03
131	26.35	0.79	47.1	5.9	3.1	1.2	8.4	2.91e+03	7.04e+03	1.7	0.4	3.28e+00	1.12e+02
133	26.55	-0.31	107.7	3.9	8.5	2.0	16.1	2.59e+04	4.48e+04	1.9	1.8	2.82e+02	3.13e+03
134	26.60	0.01	26.8	7.0	13.4	2.5	25.8	9.47e+04	1.49e+05	2.8	3.6	1.35e+03	1.02e+04
135	26.66	0.01	99.6	4.1	9.1	3.3	38.5	1.40e+05	8.11e+04	3.0	11.4	1.38e+04	1.87e+04
136	26.68	0.52	87.2	4.5	5.2	1.6	12.2	6.62e+03	7.88e+03	1.7	1.6	1.40e+02	9.37e+02
137	26.68	0.01	111.2	3.8	7.6	1.0	12.5	9.75e+03	6.97e+03	1.1	3.3	6.31e+02	2.14e+03
138	26.93	0.13	92.4	4.4	5.5	1.7	16.9	2.38e+04	3.05e+04	1.6	1.8	2.24e+02	1.38e+03
139	27.00	-0.39	68.1	5.0	4.3	1.8	6.1	2.45e+03	2.55e+03	1.8	2.8	5.81e+02	1.34e+03

Table 1—Continued

SRBY	Within SRBY Defined Area, A <sub>1</sub>									Within Half Max Isophote of N(H <sub>2</sub> ), A <sub>2</sub>			
	$l$ (deg)	$b$ (deg)	$v_o$ (km/s)	$R_g$ (kpc)	Dist (kpc)	$\sigma_v$ (km/s)	R (pc)	$L_{CO}$ ( $Kkm/spc^2$ )	$M_{LTE}$ ( $M_\odot$ )	$\sigma_v$ (km/s)	R (pc)	$L_{CO}$ ( $Kkm/spc^2$ )	$M_{LTE}$ ( $M_\odot$ )
140	26.90	-0.11	79.8	4.7	5.0	1.6	17.7	9.50e+03	1.42e+04	1.9	3.2	7.61e+02	2.85e+03
141	27.04	-0.15	102.8	4.1	9.0	1.4	14.8	2.18e+04	1.85e+04	1.4	3.0	5.08e+02	2.72e+03
142	27.24	0.14	33.3	6.6	12.9	2.6	29.0	8.54e+04	1.32e+05	2.4	5.1	2.83e+03	2.46e+04
143	27.32	-0.28	74.2	5.0	4.5	3.2	10.5	7.50e+03	6.45e+03	2.6	3.4	8.48e+02	1.81e+03
144	27.35	-0.15	92.4	4.4	5.6	1.6	9.2	1.13e+04	1.66e+04	1.5	1.1	1.26e+02	1.54e+03
145	27.52	0.21	35.4	6.5	12.7	1.0	17.0	2.46e+04	1.88e+04	1.1	2.6	5.75e+02	2.21e+03
146	27.50	0.14	97.5	4.3	9.3	3.6	23.3	8.86e+04	1.55e+05	4.1	10.4	1.78e+04	5.47e+04
147	27.63	0.10	82.9	4.7	5.1	1.5	15.0	1.71e+04	2.19e+04	1.8	0.7	3.15e+01	5.57e+02
148	27.73	0.10	98.3	4.2	8.9	3.7	37.2	1.20e+05	2.48e+05	3.4	9.9	1.29e+04	4.72e+04
149	28.19	-0.04	97.8	4.4	9.2	1.3	19.5	8.26e+04	8.32e+04	1.5	3.4	1.27e+03	9.21e+03
150	28.24	-0.38	45.9	6.0	3.0	1.8	13.8	9.51e+03	2.60e+04	2.0	0.7	3.54e+01	5.92e+02
151	28.32	-0.06	78.0	4.8	5.0	3.5	24.3	9.22e+04	2.23e+05	3.3	4.7	4.07e+03	1.70e+04
152	28.61	0.05	101.3	4.3	8.8	4.1	26.5	1.48e+05	2.16e+05	4.4	4.4	4.24e+03	1.87e+04
153	28.79	0.19	81.9	4.9	10.1	3.2	16.6	5.08e+04	6.74e+04	3.1	8.1	8.35e+03	3.04e+04
154	28.80	-0.26	87.7	4.6	5.3	0.8	16.3	5.09e+04	3.15e+04	1.1	2.2	5.95e+02	4.21e+03
155	28.98	-0.27	93.9	4.5	5.7	2.5	31.6	7.30e+04	1.82e+05	3.5	3.4	1.94e+03	1.47e+04
156	28.99	-0.67	51.1	5.9	3.3	1.9	9.4	4.26e+03	9.35e+03	1.6	1.6	1.66e+02	1.73e+03
157	29.35	-0.46	78.7	5.0	4.7	2.5	23.8	7.22e+04	9.68e+04	2.8	1.3	4.46e+02	1.98e+03
158	29.01	0.05	96.9	4.4	8.9	2.9	41.1	1.90e+05	3.74e+05	3.0	3.5	1.64e+03	7.12e+03
159	29.32	-0.57	63.9	5.4	4.0	1.7	14.0	1.49e+04	2.82e+04	1.8	4.5	1.36e+03	7.51e+03
160	29.50	0.17	79.6	4.9	4.8	2.4	19.9	3.31e+04	5.87e+04	2.4	8.5	9.00e+03	2.87e+04
161	29.61	-0.61	75.6	5.0	10.2	2.9	40.8	1.45e+05	2.69e+05	2.0	6.1	2.54e+03	2.67e+04
162	29.89	-0.06	99.0	4.4	8.5	4.5	34.9	2.81e+05	8.28e+05	4.1	6.0	1.14e+04	1.17e+05
163	29.90	0.10	39.3	6.4	12.2	2.1	12.9	1.75e+04	3.45e+04	2.0	7.0	3.33e+03	1.56e+04
164	29.91	-0.77	83.7	4.8	5.1	1.1	13.2	6.72e+03	2.04e+04	1.2	0.9	3.96e+01	1.44e+03
165	30.41	0.46	45.1	6.2	2.8	1.2	5.0	1.39e+03	1.67e+03	1.4	1.4	1.45e+02	6.63e+02
167	30.56	0.32	92.2	4.5	8.7	1.9	26.1	9.42e+04	8.70e+04	1.9	2.5	3.05e+02	2.37e+03
168	30.57	-0.02	40.8	6.3	11.9	2.9	44.7	1.47e+05	2.69e+05	3.0	2.8	8.95e+02	1.07e+04
169	30.61	-0.45	94.0	4.6	8.8	2.4	14.4	4.99e+04	3.35e+04	2.5	8.6	1.18e+04	3.81e+04
170	30.59	-0.11	115.5	4.3	7.3	0.8	19.4	3.54e+04	3.17e+04	1.1	1.7	1.67e+02	1.90e+03
171	30.77	-0.01	94.2	4.6	5.7	6.8	41.8	3.17e+05	1.10e+06	5.7	5.2	1.11e+04	7.59e+04
172	30.83	-0.18	51.6	5.9	3.3	1.8	8.8	3.06e+03	6.90e+03	1.5	0.4	6.16e+00	3.12e+02
173	30.89	-0.60	102.0	4.4	7.9	0.7	8.4	6.67e+03	2.61e+03	0.9	2.2	3.23e+02	7.74e+02
174	30.96	0.09	39.5	6.5	12.1	3.3	36.2	1.30e+05	2.22e+05	2.1	3.3	1.07e+03	6.60e+03

Table 1—Continued

SRBY	Within SRBY Defined Area, A <sub>1</sub>									Within Half Max Isophote of N(H <sub>2</sub> ), A <sub>2</sub>			
	$l$ (deg)	$b$ (deg)	$v_o$ (km/s)	$R_g$ (kpc)	Dist (kpc)	$\sigma_v$ (km/s)	R (pc)	$L_{CO}$ ( $Kkm/spc^2$ )	$M_{LTE}$ ( $M_\odot$ )	$\sigma_v$ (km/s)	R (pc)	$L_{CO}$ ( $Kkm/spc^2$ )	$M_{LTE}$ ( $M_\odot$ )
175	30.97	0.40	79.7	5.1	4.7	2.6	12.5	2.13e+04	3.96e+04	2.3	1.1	1.04e+02	1.08e+03
177	31.28	-0.00	79.7	5.0	4.9	3.2	14.7	2.66e+04	4.84e+04	3.2	5.4	3.96e+03	1.48e+04
178	31.32	-0.03	41.0	6.6	12.1	3.7	58.6	2.43e+05	5.06e+05	3.5	7.7	5.88e+03	4.31e+04
179	31.39	-0.26	87.9	4.8	9.1	1.6	13.6	1.84e+04	1.63e+04	1.7	2.8	6.69e+02	4.06e+03
180	31.44	0.08	106.0	4.4	7.3	2.6	21.9	6.62e+04	8.94e+04	3.0	3.2	1.77e+03	1.31e+04
181	31.98	-0.28	97.5	4.6	8.1	2.5	19.0	3.62e+04	3.08e+04	2.6	7.4	5.03e+03	1.28e+04
182	32.02	0.06	96.8	4.6	8.0	2.1	37.7	8.93e+04	1.57e+05	2.5	3.3	1.91e+03	1.54e+04
183	32.46	0.22	50.6	6.1	11.2	1.4	15.0	2.20e+04	4.02e+04	1.5	2.0	2.40e+02	3.39e+03
184	32.70	-0.18	92.5	4.8	8.6	1.7	44.4	1.58e+05	1.38e+05	1.5	3.0	7.47e+02	5.32e+03
185	33.38	-0.53	91.2	4.8	8.2	1.6	23.0	2.24e+04	2.81e+04	1.5	6.3	2.41e+03	8.63e+03
186	33.36	-0.00	72.9	5.3	9.6	2.4	34.0	8.36e+04	1.06e+05	2.2	5.5	3.46e+03	9.11e+03
187	33.44	-0.08	86.5	4.9	8.7	2.2	35.7	8.99e+04	1.14e+05	2.2	11.4	9.66e+03	2.40e+04
188	33.79	-0.18	52.4	6.3	11.2	3.4	32.9	6.16e+04	1.16e+05	3.1	5.6	2.71e+03	1.16e+04
189	33.66	0.22	41.7	6.5	11.6	1.5	21.3	2.41e+04	3.11e+04	1.2	3.3	4.22e+02	3.04e+03
190	33.85	0.00	89.2	4.9	8.4	1.2	19.9	3.48e+04	2.48e+04	1.2	12.1	8.33e+03	1.44e+04
191	33.83	0.07	105.6	4.7	7.1	2.2	30.1	6.69e+04	7.76e+04	2.0	2.1	4.74e+02	2.83e+03
192	34.16	-0.10	88.1	4.9	8.3	2.1	21.5	4.01e+04	3.56e+04	1.9	6.0	2.26e+03	9.18e+03
193	34.20	0.12	57.5	6.1	3.2	2.8	18.1	3.00e+04	1.07e+05	2.8	1.4	1.68e+02	1.70e+04
195	34.36	-0.19	52.2	6.1	3.2	2.3	7.6	3.37e+03	7.86e+03	2.3	2.7	5.94e+02	2.58e+03
196	34.76	-0.13	78.9	5.3	4.8	3.3	16.1	1.59e+04	3.37e+04	3.6	3.7	1.32e+03	5.67e+03
198	34.99	0.33	51.8	6.2	3.1	1.0	15.7	2.31e+04	3.60e+04	1.3	0.7	4.54e+01	8.03e+02
202	35.66	0.15	81.7	5.2	8.5	2.7	36.0	9.81e+04	1.43e+05	2.2	2.1	3.41e+02	4.21e+03
203	35.79	-0.16	28.8	7.2	1.7	1.2	12.8	3.80e+03	7.76e+03	0.9	0.6	6.14e+00	5.66e+02
204	35.97	-0.48	58.7	6.0	3.5	1.7	6.4	3.69e+03	4.50e+03	1.6	2.5	4.44e+02	2.00e+03
205	36.13	0.66	77.5	5.4	4.9	3.6	31.7	5.58e+04	7.36e+04	2.2	1.5	1.91e+02	1.30e+03
206	36.42	-0.10	54.8	6.3	3.1	2.0	17.2	2.74e+04	5.13e+04	1.8	3.6	9.23e+02	5.00e+03
207	36.49	-0.11	78.6	5.4	4.9	3.1	25.3	3.51e+04	5.95e+04	2.3	2.0	2.90e+02	2.10e+03
208	36.90	-0.07	79.9	5.3	5.2	2.2	13.9	1.81e+04	3.66e+04	2.1	6.4	4.24e+03	1.58e+04
209	37.38	0.17	87.2	5.2	6.8	3.1	31.8	7.05e+04	1.24e+05	2.7	1.4	1.02e+02	5.27e+03
210	37.49	0.08	41.9	6.7	2.4	1.6	6.4	1.92e+03	2.95e+03	0.9	0.5	3.97e+00	2.92e+02
211	37.76	-0.21	62.8	6.0	9.8	3.4	20.8	5.01e+04	7.71e+04	3.1	3.2	1.14e+03	8.41e+03
212	38.23	-0.15	62.9	5.9	9.3	2.7	10.8	2.13e+04	3.16e+04	2.9	5.1	2.78e+03	1.38e+04
213	38.93	-0.45	41.7	6.8	2.5	1.5	10.8	9.17e+03	2.28e+04	1.4	1.0	1.52e+02	1.29e+03
214	39.83	-0.28	60.3	6.2	9.6	3.8	90.8	7.72e+05	1.19e+06	3.4	15.1	2.81e+04	1.08e+05

Table 1—Continued

SRBY	Within SRBY Defined Area, A <sub>1</sub>									Within Half Max Isophote of N(H <sub>2</sub> ), A <sub>2</sub>			
	$l$ (deg)	$b$ (deg)	$v_o$ (km/s)	$R_g$ (kpc)	Dist (kpc)	$\sigma_v$ (km/s)	R (pc)	$L_{CO}$ ( $K\text{ km/spc}^2$ )	$M_{LTE}$ ( $M_\odot$ )	$\sigma_v$ (km/s)	R (pc)	$L_{CO}$ ( $K\text{ km/spc}^2$ )	$M_{LTE}$ ( $M_\odot$ )
215	40.32	-0.42	73.5	5.7	5.0	0.9	12.5	8.05e+03	8.35e+03	1.0	1.2	5.75e+01	5.59e+02
216	41.05	-0.17	39.8	7.0	2.2	1.8	11.4	8.01e+03	1.29e+04	1.9	3.5	7.76e+02	3.28e+03
217	41.18	-0.22	61.1	6.2	9.0	1.8	42.6	1.99e+05	2.52e+05	1.5	1.5	1.98e+02	3.73e+03
218	41.89	-0.40	60.3	6.2	8.9	1.4	25.3	5.69e+04	6.72e+04	1.6	5.8	2.60e+03	9.71e+03
219	42.34	-0.08	57.5	6.3	8.9	3.0	20.6	5.06e+04	6.33e+04	2.7	3.5	1.11e+03	4.59e+03
220	42.15	-0.60	67.2	6.0	4.5	2.2	15.9	2.84e+04	5.52e+04	1.7	0.3	4.58e+00	3.59e+02
221	42.72	-0.35	62.6	6.3	3.8	3.8	16.9	1.97e+04	5.74e+04	3.5	1.5	1.46e+02	1.11e+03
223	43.17	-0.52	57.9	6.4	3.6	1.2	7.1	2.56e+03	6.79e+03	1.5	0.5	2.22e+01	1.34e+03
224	44.38	-0.22	61.2	6.2	7.7	4.0	46.1	1.91e+05	4.59e+05	2.3	0.8	4.67e+01	2.68e+03
225	45.44	0.07	59.9	6.4	8.1	4.4	47.0	1.66e+05	4.43e+05	3.0	3.6	2.03e+03	2.03e+04
226	46.32	-0.20	55.0	6.4	7.7	3.4	13.6	1.42e+04	5.82e+04	2.5	1.5	1.41e+02	3.43e+03
227	47.05	0.26	57.6	6.6	7.9	2.1	19.8	2.15e+04	6.81e+04	1.7	2.2	2.63e+02	1.29e+04
229	47.55	-0.54	59.1	6.4	7.2	1.7	17.7	1.97e+04	1.95e+04	1.6	3.7	5.69e+02	3.32e+03
232	48.83	0.14	52.6	6.7	7.7	1.9	32.0	3.42e+04	1.28e+05	1.5	2.0	2.25e+02	2.98e+03
234	49.74	-0.52	68.1	6.5	5.5	1.1	11.9	9.88e+03	1.89e+04	0.9	2.7	4.92e+02	2.61e+03
236	50.83	0.25	42.3	7.0	2.9	2.0	7.3	2.62e+03	7.69e+03	1.6	0.7	1.79e+01	7.96e+02
237	51.33	-0.04	54.7	6.7	6.2	2.5	31.3	6.05e+04	9.99e+04	1.9	0.8	4.53e+01	4.28e+03
238	52.30	-0.06	51.1	6.8	6.1	1.6	12.3	1.38e+04	1.90e+04	1.6	5.2	1.63e+03	6.23e+03
240	53.17	-0.25	62.7	6.8	5.1	2.3	9.0	8.71e+03	1.28e+04	1.9	1.3	1.32e+02	1.37e+03
241	53.43	0.07	23.3	7.7	1.5	1.1	15.9	5.19e+03	2.26e+04	0.9	0.2	6.26e+00	2.72e+02
242	54.12	-0.07	39.1	7.2	7.0	2.5	12.8	1.24e+04	5.03e+04	2.3	3.5	1.84e+03	1.95e+04
243	54.66	0.81	32.8	7.5	7.7	2.9	28.2	4.33e+04	1.12e+05	2.8	7.3	5.11e+03	2.17e+04